https://doi.org/10.5194/wes-2026-160
Preprint. Discussion started: 14 September 2026

Open Access
WIND ENERGY SCIENCE DISCUSSIONS

Effect of inflow turbulence on the wake replenishment mechanisms of twin rotor vertical axis wind turbine

Querat Simon[a,b], Augier Benoît[a], Träsch Martin[a], Germain Grégory[a], Barre Stephane[c], Delon Antoine[b], and Minguez Matthieu[b]

[a]RDT Research and Technological Development, Ifremer, 1625 Rte de Sainte-Anne 29280 Plouzané, France
[b]BlueTwin, 57 Allée Frédéric Desmons, 30000 Nîmes, France
[c]LEGI, 1209 Rue de la Piscine, 38610 Gières, France

Correspondence: Augier Benoît (benoit.augier@ifremer.fr)

Abstract.

The effect of inflow turbulence on wind turbine's wake replenishment has been well observed in the scientific literature. The turbulent mixing is frequently proposed to explain the faster wake replenishment in turbulent condition. In order to verify this assumption, the wake of a twin rotor vertical axis wind turbine has been studied in two conditions with different inflow turbulence levels. The 1/450 scale model was immersed in a flume tank and velocity measurements were performed with a LDV probe. The terms of the momentum budget equation were computed in order to find those responsible for the wake replenishment. The vertical advection term has been found to be the major contributor of the transport of momentum in the wake, in accordance with the literature. However, in contradiction with previous assumptions, the turbulent transport terms were not found to have a significant effect on the wake replenishment. The earlier onset of the vertical advection is identified has the main explanation for the ter wake replenishment in the turbulent condition. Finally, the cause of this earlier onset is studied in order to analyse how the vertical turbulence gradient plays a role or not on this process.

1 Introduction

Wind turbines are commonly arranged in large wind farms. This configuration is chosen to facilitate the grid connection and marine servicing operation, as well as to reduce the surface area occupied by wind turbines in order not to disturb other activities. Although it has a great impact on the overall power production of the farm, as the downstream wind turbines are impacted by the wake of the upstream ones. Several solutions have been proposed to reduce the power loss of the wind farms due to the wake effects. These solutions can involve modifying the control of the turbine, such as rotor misalignment (Bromm et al., 2018) or leap-frogging activation by pitching (Brown et al., 2022). They can also involve changing the wind turbine design.

https://doi.org/10.5194/wes-2026-160
Preprint. Discussion started: 14 September 2026

eawe european academy of wind energy
Open Access WIND ENERGY SCIENCE DISCUSSIONS

With the development of floating application, vertical axis wind turbine (VAWT) are gaining interest. This is due to several advantages, such as the lower center of mass and thurst application point (Matoug et al., 2020) and the easier maintenance with the generator placed near the sea level Achard et al. (2017). Numerical studies tend to show that this design could also help reduce the wake power loss in the wind farms thanks to their potential for a faster wake recovery (Boudreau and Dumas, 2017). But this result lacks of experimental validation.

Characterising the wake replenishment mechanisms and its sensitivity to inflow condition is challenging due to the extensive tests that are required. However, these results are crucial in order to both propose relevant solutions to reduce wake effects and to design efficient wind farms layout, taking into account the site conditions. One of the inflow condition that has the most important effect on the wake is the turbulence intensity level (Wang et al., 2021). For both VAWT and horizontal axis wind turbine (HAWT), the effect of inflow turbulence has often been observed (van der Deijl et al., 2024; Chu and Chiang, 2014; Peng and Lam, 2016; Dabiri, 2011). In both cases, high inflow turbulence intensity leads to faster wake recovery. As the fluctuating terms of the velocity is involved in the momentum transport inside the wake, the turbulence is frequently proposed to explain the faster wake recovery. However, to the author's best knowledge, this explanation has never been verified for VAWT.

By computing the terms of the momentum budget equation, recent studies have been able to experimentally identify the terms responsible for the wake replenishment (Bachant and Wosnik, 2015; Talamalek et al., 2024; Rolin and Porté-Agel, 2018; Ouro et al., 2019). They show that the momentum transport by mean velocity is greater than the turbulent transport, especially the vertical advection term which has been found to be the major contributor of momentum transport. As these studies were performed for only one inflow condition, the effects of inflow turbulence are not observed. Up to this day, only one study performed a similar analysis with two inflow turbulence levels (Talamalek et al., 2025) . Unfortunately, in this particular case the higher turbulence intensity didn't lead to a faster wake recovery. Therefore they were not able to conclude on the effect of inflow turbulence on the wake replenishment mechanisms.

In this work, a twin-rotor O-shaped vertical axis wind turbine is immersed in a flume tank. The wind turbine is developed by the BlueTwin company for floating applications. Velocity measurements are performed in cross-stream planes at different downstream distances with a 3 components Laser Doppler Velocimetry (LDV) probe. The terms of the momentum budget equation can then be computed, allowing their contribution to the momentum transport to be quantified for all measurement planes. This experiment has been conducted for two inflow conditions with different turbulence levels. In a first part, the test facilities and the flow characteristics are presented, and the processing method are described. In a second part the velocity deficit, the turbulent kinetic energy and the wake replenishment mechanisms for both inflow conditions are presented and compared. In a third part, the phenomenon responsible for the faster wake recovery is identified and discussed.

2 Description of the experimental setup and flow characteristics

In this section, the test facilities, the wind turbine model design and the instrumentation are presented. Then, the flow characteristics and the post-processing methods that are used are described.

https://doi.org/10.5194/wes-2026-160
Preprint. Discussion started: 14 September 2026

The experiment took place in the Ifremer Boulogne-sur-Mer flume tank presented figure 1a. This choice has been made as this facility offers the velocity and turbulence intensity (TI) profiles required for this study and because velocity measurements are more convenient in water, while in this case the physics remains the same in air and water. The test section is 4 meters wide and 2 meters high. The length of the test section is 8 meters, with 10 meters between the honeycomb and the inlet of the test section. A movable floor enables to install experimental models in the test section.

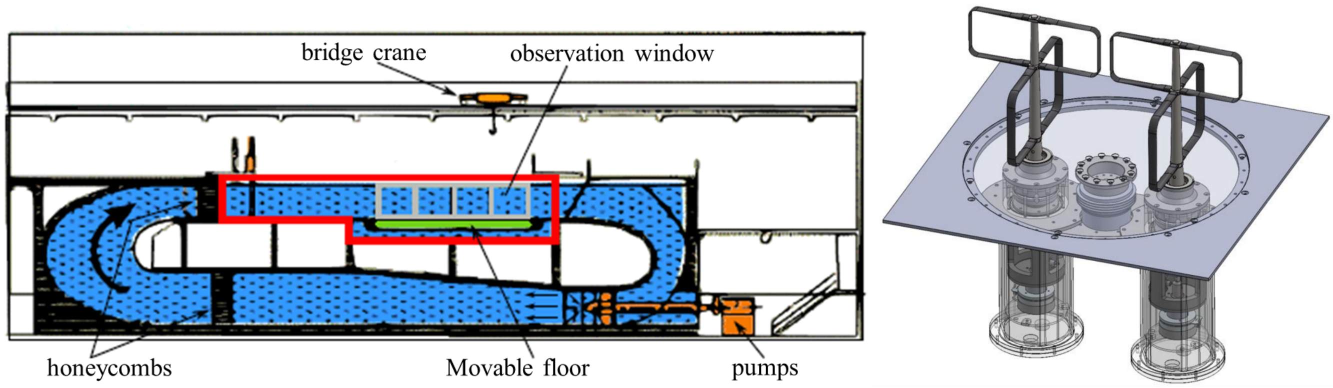

(a) (b)

Figure 1. Schematic view of the Ifremer Boulogne-sur-Mer flume tank (a). Schematic view of the wind turbine scale model. The gears, the motors, the load and torque sensors are under the movable floor (b).

The twin-rotor vertical axis wind turbine scale model used in this study is presented in figure 1b. Each rotor consists of two stages angularly offset by 90°. Each stage is a two-bladed O-shape rotor. Table 1 summarizes the geometric parameters of the model. The wind turbine is in an inner-downwind configuration. It is fixed on a SIXAXES 1.5 kN 6-component load cell. The electronic systems are installed in two watertight blocks located under the two columns. Each block comprises a Maxon RE50 200W motor equipped with a 1/26th gear reducer and a speed encoder. The load cell and the watertight blocks are placed under the bottom floor of the tank without any interaction with the flow. The motors are piloted using remote EP OS2 servo-controllers in constant speed mode. The two rotors are not angularly synchronized.

The tip speed ratio (TSR) of the rotors is given by the equation 1 with $R = \frac{D}{2}$ and ω the rotational speed of the turbine. The whole experiment is performed at the turbine optimal TSR of 3.7. Both columns operate at the same TSR.

$$TSR = \frac{R\omega}{U_0} \tag{1}$$

During the tests, the continuous operation of the pumps caused the water to warm up by about 1°C per day. This temperature variation has an impact on the kinematic viscosity of the water and therefore the Reynolds number. The diameter based Reynolds number is given by equation 2 with ρ the density and μ the dynamic viscosity of the fluid. Over all the tests, the Reynolds number stayed between $4.25 \cdot 10^5$ and $4.83 \cdot 10^5$.

https://doi.org/10.5194/wes-2026-160
Preprint. Discussion started: 14 September 2026

Parameter	Symbol	Value
Diameter	D	335mm
Total height	H	335mm
Stage 1 height	H1	205mm
Stage 2 height	H2	130mm
Angular offset	none	90°
Number of blades	N	2
Chord	C	21mm
Axes spacing	E	369mm
Air gap	G	50mm
Profile	none	NACA0018

Table 1. Geometrical parameter of the model.

$$Re_D = \frac{\rho U_0 D}{\mu} \tag{2}$$

The thrust coefficient C_T is calculated using the expression 3, with T the drag force, ρ the density of the water and S the surface area of the rotors. The drag force was measured with the load cell for the low turbulence case, but the measurement could not be repeated for the high turbulence case because of a load sensor failure. In the present turbulence intensity range, the inflow turbulence intensity does not affect the thrust coefficient (Magnier, 2023). At TSR=3.7, the thrust coefficient is $C_T = 0.72$.

$$C_T = \frac{T}{\frac{1}{2}\rho S U_0^2} \tag{3}$$

The velocity is measured with a Dantec Dynamics 3 components LDV probe. The flow is seeded with 0.01mm diameter silver coated hollow glass spheres. The probe has been designed for Ifremer Boulogne-sur-Mer flume tank and is composed of one vertical two components probe that measures directly u and v and one angulated one component probe that measures a component composed by u and w. Figure 2a shows the LDV 3C probe in the measurement process. The blue lasers are from the LDV 2C probe and the green lasers are from the LDV 1C probe. The travelling of the probe is automated for Y and Z axis, allowing for fully automated cross-stream plane wake measurements.

In the flume tank, the velocity and turbulence intensity profile can be changed by using different grids composed of specific metal mesh assembly placed before the honeycomb. Here, two grids are used to observe the effect of turbulence on turbine wake dissipation. The two grids have similar porous part with only the addition of a 20cm-high solid plate at the bottom for turbulence generation. The geometry of the grids is presented in figure 2b (Magnier, 2023).

Figure 3a shows the velocity profiles measured by LDV for both grids. Atmospheric Boundary Layer (ABL) velocity profile can be approximated by power law (VDI, 2000). This law is given by equation 4 with $\overline{u}$ the mean velocity, z the altitude

https://doi.org/10.5194/wes-2026-160
Preprint. Discussion started: 14 September 2026

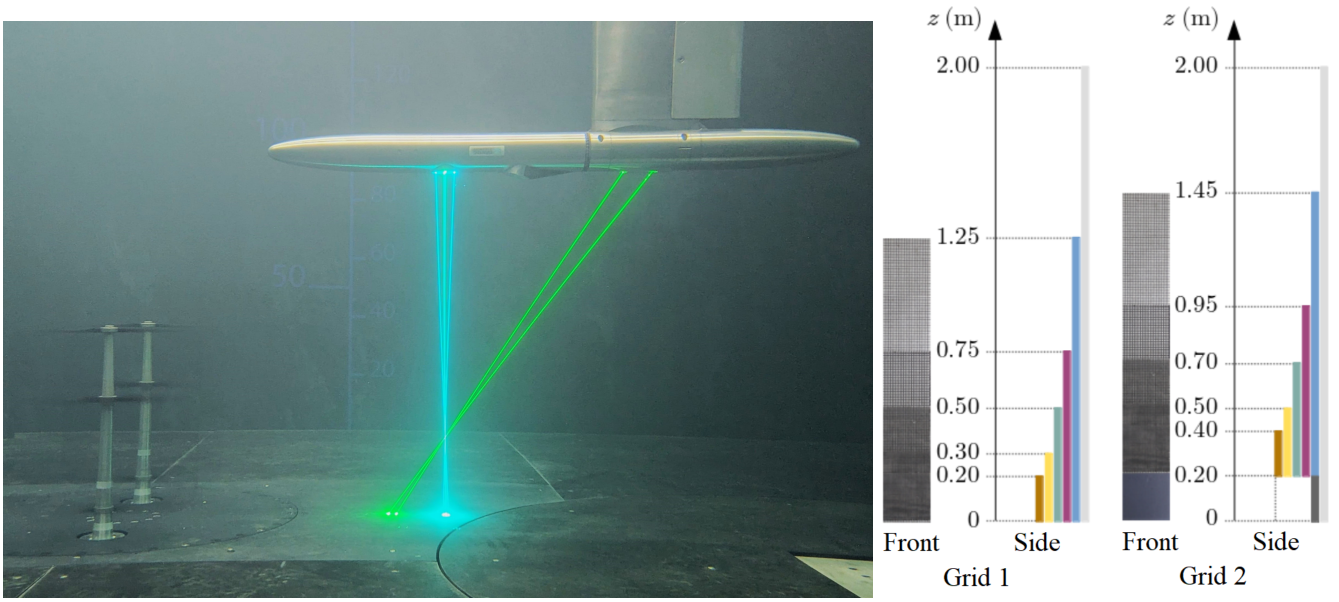

(a) (b)

Figure 2. The LDV 3C probe in measurement process in the wake of the wind turbine (a). Geometry of the two grids composed of a metal mesh assembly. (b).

over ground and u_0 the reference velocity at the reference altitude z_0. A linear fitting is performed between $0 < z < 2H$ after applying the logarithm. The result are $\alpha = 0.13$ for grid 1 and $\alpha = 0.15$ for grid 2, with good coefficients of determination. These exponents correspond to the low limit for an ABL over low rugosity terrain.

$$\overline{u} = u_0 \left(\frac{z}{z_0}\right)^{\alpha} \tag{4}$$

For the same velocity setpoint, the profile obtained with grid 2 results in a 10% lower flow rate velocity over the height of the turbine compared with the grid 1 profile. The rotation speed of the rotors were then adjusted in order for the two campaigns to be run at the optimal TSR.

The components of the turbulence intensity are calculated using the equation 5. $\sigma()$ is the standard deviation operator, u, v and w are the 3 components of the velocity at a measurement point, and U_0 is the flow rate velocity over the height of the turbine, given by the equation 6.

$$TI_x = \frac{\sigma(u)}{U_0} \qquad TI_y = \frac{\sigma(v)}{U_0} \qquad TI_z = \frac{\sigma(w)}{U_0} \tag{5}$$

https://doi.org/10.5194/wes-2026-160
Preprint. Discussion started: 14 September 2026

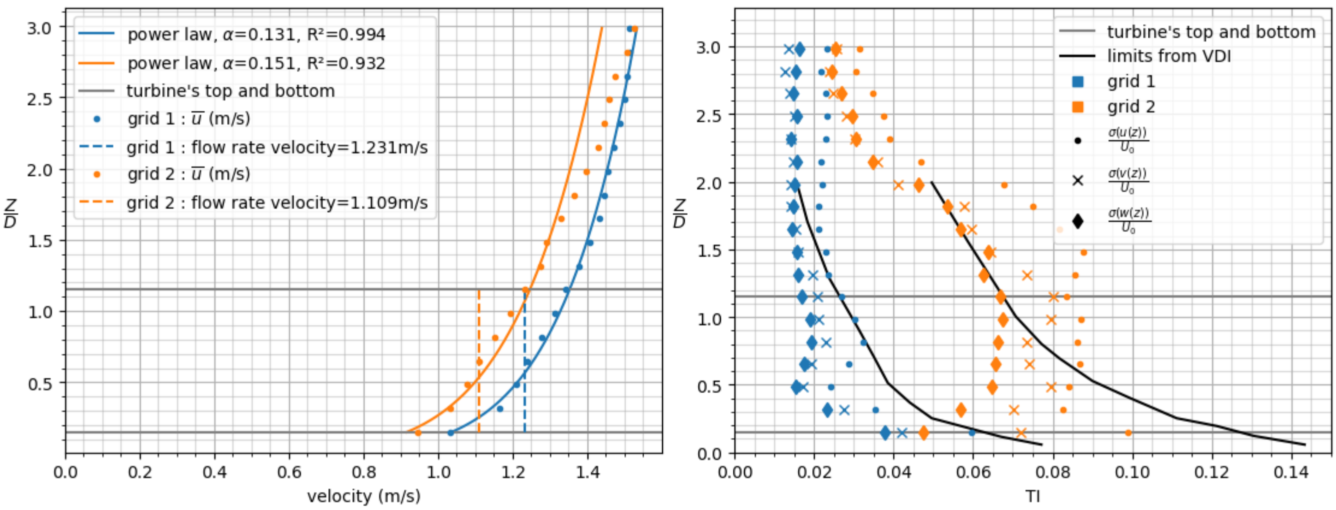

(a) (b)

Figure 3. Vertical velocity (a) and turbulence intensity (b) profiles of the two configurations studied.

$$U_0 = \frac{1}{H} \int_{G}^{H+G} \overline{u(z)} dz \tag{6}$$

Turbulence intensity components profiles obtained with the two grids are presented in figure 3b. The longitudinal turbulence intensity of 3% obtained with grid 1 is in the lower limit of what is encountered at sea. The turbulence intensity of 8% obtained with grid 2 is a turbulence intensity which is in the upper limit of what can be encountered at sea at 39 m (Thilleul and Perignon, 2022) and at 140 m (Thiébaut et al., 2024). The limits for an offshore ABL are plotted in figure 3b. The two conditions studied here embrace the range proposed by the VDI (VDI, 2000). The turbulence intensities along Y and Z are also shown in the figure. They are lower than the longitudinal turbulence intensity for both grids, which is expected for a boundary layer type flow.

In the case of grid 2 with a solid plate at the bottom, the vortex shedding could affect the flow at the level of the wind turbine. Especially if the latter is not placed far enough downstream from the grid. Here, the wind turbine is located at a distance equivalent to 50 times the height of the obstacle. This would result in a low frequency turbulence component that can affect the wake of the wind turbine. To verify the absence of this component, the power spectral densities for the two grids is plotted for different heights figure 4. The energy level is generally higher for grid 2, and no peak is visible. It is concluded that at this distance downstream of the obstacle, the fluctuations due to the vortex release are no longer visible and therefore have no impact on the results.

In the following, case grid 1 will be referred to as the low turbulence case, and case grid 2 will be referred to as high turbulence case. Table 2 resume the experiment flow characteristics and turbine operating conditions.

https://doi.org/10.5194/wes-2026-160
Preprint. Discussion started: 14 September 2026

WIND ENERGY SCIENCE DISCUSSIONS
Open Access

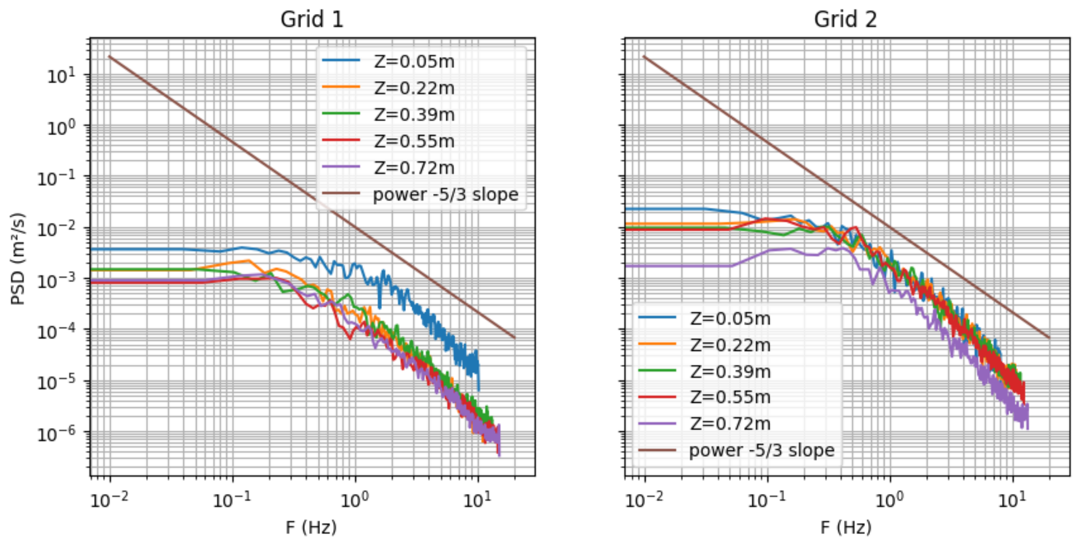

Figure 4. Power spectral densities obtained at different height for the two configurations studied.

Case	Low turbulence	High turbulence
Flow rate velocity U_0	1.23m/s	1.11m/s
Power law fitting	$\alpha = 0.13$	$\alpha = 0.15$
TI	3%	8%
Water temperature	23°C-27°C	26°C-30°C
Re_D	4.41-4.83 ($\cdot 10^5$)	4.25-4.63 ($\cdot 10^5$)
RPM	260	234
TSR	3.7	3.7
C_T	0.72	0.72

Table 2. Flow characteristics and turbine operating condition for the wake characterisation by 3C LDV measurements.

The aim of these tests is to understand the effect of upstream turbulence on the physical mechanisms involved in wake resorption. To do this, the different terms that contribute to the transport of momentum from the outside to the inside of the wake must be estimated. These terms are explained in equation 7. The demonstration of this result is presented in appendix A.

$$\frac{\partial \overline{u}}{\partial x} = \frac{1}{\overline{u}}\left[-\overline{v}\frac{\partial \overline{u}}{\partial y} - \overline{w}\frac{\partial \overline{u}}{\partial z} - \frac{1}{\rho}\frac{\partial \overline{p}}{\partial x} - \frac{\partial \overline{u'^2}}{\partial x} - \frac{\partial \overline{u'v'}}{\partial y} - \frac{\partial \overline{u'w'}}{\partial z}\right] + \frac{1}{\overline{u}}\left[\nu\left(\frac{\partial^2 \overline{u}}{\partial x^2} + \frac{\partial^2 \overline{u}}{\partial y^2} + \frac{\partial^2 \overline{u}}{\partial z^2}\right)\right] \tag{7}$$

The viscosity transport term $\frac{\nu}{\overline{u}}\left(\frac{\partial^2 \overline{u}}{\partial x^2} + \frac{\partial^2 \overline{u}}{\partial y^2} + \frac{\partial^2 \overline{u}}{\partial z^2}\right)$ is negligible as the Reynolds number is high far from the walls. The pressure gradient $-\frac{1}{\overline{u}\rho}\frac{\partial \overline{p}}{\partial x}$ cannot be calculated because the pressure was not measured. The turbulent kinetic energy production $-\frac{1}{\overline{u}}\frac{\partial \overline{u'^2}}{\partial x}$ cannot be calculated in this work because of the large distances between the measurement points along X. However,

https://doi.org/10.5194/wes-2026-160
Preprint. Discussion started: 14 September 2026

Stream wise distances	2D, 4D, 6D, 10D
Displacement step	D/6
Plane size	2D×2H
Number of points	13×14pts
Measurement time	3min

Table 3. Parameters used for the 3C LDV measurements

according to the thin layer approximation, they are assumed to be negligible compared to the lateral gradients. Neither the pressure gradient nor the turbulent kinetic energy are calculated in the literature (Talamalek et al., 2024; Bachant and Wosnik, 2015).

The terms $-\frac{\overline{v}}{\overline{u}}\frac{\partial \overline{u}}{\partial y}$ and $-\frac{\overline{w}}{\overline{u}}\frac{\partial \overline{u}}{\partial z}$ represent the transport of momentum by the mean flow, horizontal and vertical respectively, also known as horizontal and vertical advection. The terms $-\frac{1}{\overline{u}}\frac{\partial \overline{u'v'}}{\partial y}$ and $-\frac{1}{\overline{u}}\frac{\partial \overline{u'w'}}{\partial z}$ represent the transport of momentum by turbulence, horizontally and vertically respectively.

In order to correctly estimate the spatial derivatives, a sufficiently fine measurement grid must be adopted. A displacement step $dy = dz = D/6$ is adopted as it seems to be a good compromise between refinement and measurement time (Talamalek et al., 2024). The measurement plans must contain the entire wake and areas where momentum transport is high. A dimension of 2D×2H, 13×13pts is adopted, with an additional 13 points line at the bottom. Four measurement planes are made at X/D=2, 4, 6 and 10. Figure 5 shows the measurement grid and Table 3 resume the parameters of the LDV measurements.

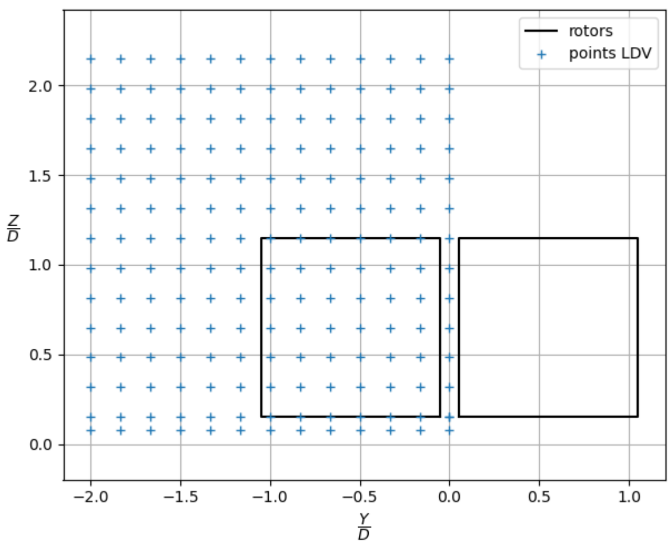

Figure 5. The measurement points in the machine's reference frame. The rotors are shown in black.

https://doi.org/10.5194/wes-2026-160
Preprint. Discussion started: 14 September 2026

A measurement time of 3 minutes has been selected as it ensure the convergence of the average and fluctuating quantities (Moreau et al., 2023). Figure 6a shows the convergence of the 3 components of the velocity and figure 6b shows the convergence of the order 2 moments over the 180 seconds of acquisition. This is done for a measurement point representative of the majority of the data with a data rate of 6.5Hz.

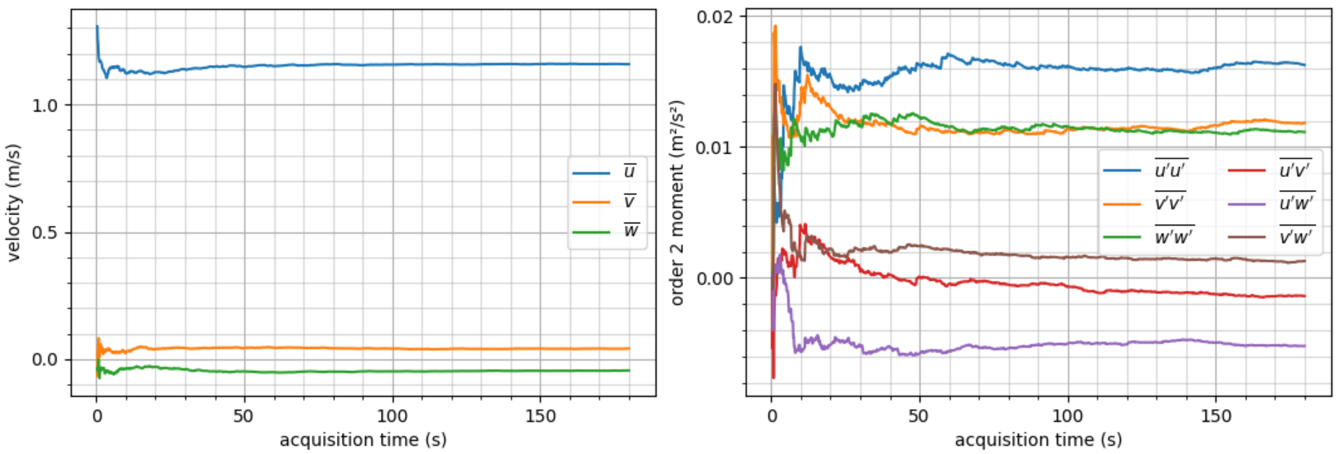

(a) (b)

Figure 6. Time average of the 3 velocity components (a) and Reynolds stress components (b) as a function of the acquisition time.

The data rate is not fixed as it is given by the number of particles passing through the focusing volume of the probe each second. Initially, the data acquisition is made separately for each component of the probe. In order to be able to calculate w wich is a composition of u and the angulated probe direction, all components must be estimated on the same time sample. Two methods were tested. In the interpolation method, the data of each component are interpolated in the time sample of the component that has the lowest data rate. In the coincidence method, the time sample of the component with the lowest data rate is also used. For each time in the sample, a measurement point is searched in the two other component's time sample within a coincidence window. If a point is found in both sample, then the point is retained. Else, the point is rejected. This process ensure that for each measurement time, the same particle is captured by the 3 components of the probe, although it has a negative impact on the data rate. Table 4 presents the average, minimum and maximum data rate for each measurement plane.

Despite the low data rate obtained with the coincidence method, it has been retained in this work for several reasons. Firstly, it was observed that the lower data rate doesn't affect the convergence of the quantities measured. Secondly, a bias in favor of high velocities can exist when the correlation between the data rate and the velocity measured is above 0.3 (Boutier, 2012). With the interpolation method, about 10% of the measurement points are above this requirement. With the coincidence method and a window of 1ms, it drops to less than 1%. Lastly, a comparison with PIV measurements shows that typical bias occurring with 3 components LDV probe (Boutier, 2012) are less important with the coincidence method. The comparison with PIV measurements carried out under the same experimental set-up shows a good agreement between 3C LDV measurements and

https://doi.org/10.5194/wes-2026-160
Preprint. Discussion started: 14 September 2026

Plane	Average (Hz)	Min (Hz)	Max (Hz)
Low turbulence case			
2D	4.52	1.01	9.17
4D	6.96	1.64	11.77
6D	10.7	3.52	18.66
10D	13.5	5.53	22.04
High turbulence case			
2D	7.01	1.82	12.6
4D	4.26	1.41	8.12
6D	2.74	1.17	5.12
10D	2.39	0.79	4.71

Table 4. Average, minimum and maximum data rates for each measurement plane for the two test cases.

2D PIV ones. This comparison is given in appendix B. These results provide good confidence in the article's conclusions regardless of the 3C LDV data processing method chosen.

3 Influence of the inflow turbulence on the wake

In this part, the wake average velocity and turbulent kinetic energy are first described. Then, the wake replenishment mechanisms through the contribution of the different terms of the momentum budget equation and more specifically the impact of the inflow turbulence level on these mechanisms are investigated. Finally, an explanation of how the inflow turbulence triggers these mechanisms is proposed.

3.1 Wake description

The average velocity mapping for low turbulence and high turbulence case are presented in figure 7. Longitudinal velocities are represented by colors and transverse velocities by vectors. In all upcoming color-map, the rotor is represented by the gray dashed lines. The horizontal arrow at the bottom of the figures represents a cross-stream velocity of $0.1U_0$. All velocities are scaled by U_0. The velocity scale is the same on both figures. The longitudinal velocity recovers more quickly in the turbulent sheared case. In both cases, a significant downward vertical velocity is observed. This vertical velocity is already in place at $X = 2D$ in the high turbulence case, whereas it does not appear until $X = 4D$ in the low turbulence case. It also fades out earlier in the high turbulence case.

Figure 8 compares the averaged velocity over a reference surface as a function of downstream distance of the wind turbine between the low and high turbulence case. The reference surface must contain all the areas of high momentum transport and must not be too large to avoid attenuating the data with areas of very low momentum transport (Talamalek et al., 2024). Here the reference surface chosen is delimited by $-1.5D < Y < 0$ and $0.075D < Z < 1.5D$. At $X/D = 2$, the mean surface velocities

https://doi.org/10.5194/wes-2026-160
Preprint. Discussion started: 14 September 2026

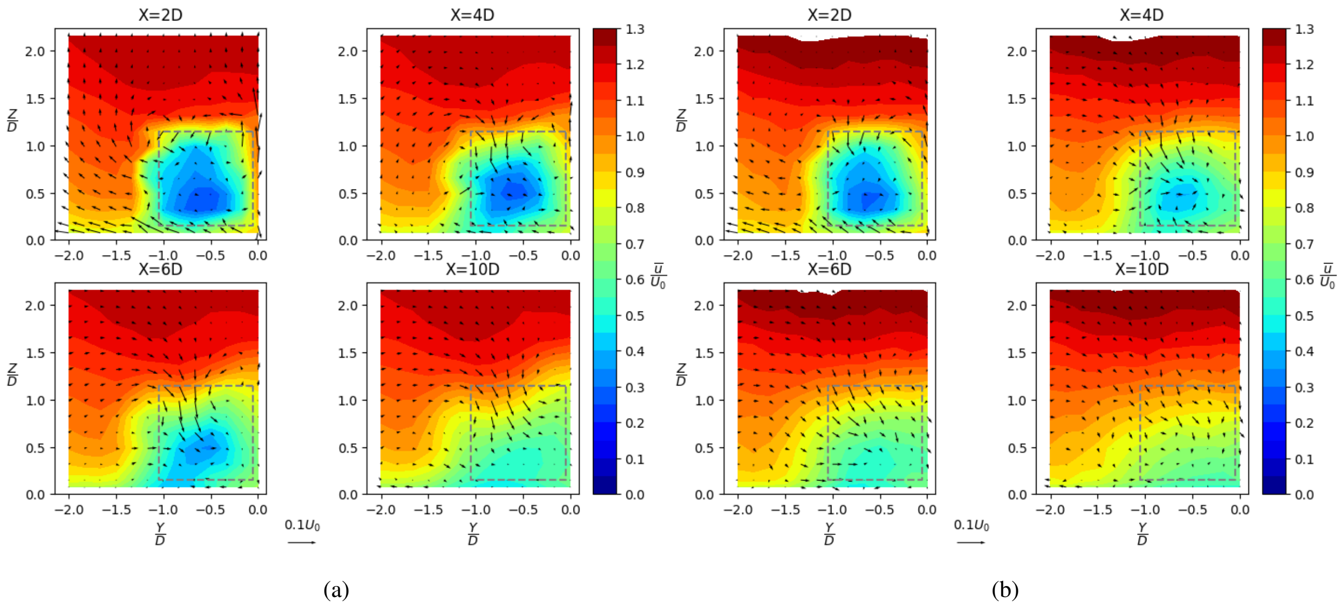

Figure 7. Velocity map for the low turbulence case (a) and high turbulence case (b). The colors represent the axial velocity, the arrows represent the cross-stream velocity. The dashed gray lines represent the rotors.

are close for both cases. Between $X/D = 2$ and $X/D = 6$, the recovery rate is higher in the high turbulence case. After $X/D = 6$, the recovery rates are similar. Finally, at $X/D = 10$ the mean velocity on the reference surface is $< U >= 0.795U_0$ for the low turbulence case and $< U >= 0.857U_0$ for the high turbulence case.

In order to compares global turbulence level of the two cases, the turbulent kinetic energy (TKE) is mapped in figure 9. The arrows represent the cross-stream velocities. In both cases, the TKE first develops at the edges of the wake in the most sheared area. Then it spreads from the outside towards the inside of the wake. The TKE in the wake is higher in the high turbulence case. This is consistent with the results obtained in the literature (van der Deijl et al., 2024; Talamalek et al., 2025). Figures C1 to C3, presented in appendix C show that the areas of high Reynolds normal stress are evenly distributed on the borders of the wake in the near wake. Further downstream theses areas spread toward the core of the wake. The same behavior is encountered for the three Reynolds normal stress components with a factor 2 between the low and the high turbulent cases. Figures C4 to C6 shows that the X-Y Reynolds shear stress is high on the sides of the wake. The X-Z Reynolds shear stress is high on the top and bottom of the wake. They also tend to spread toward the core of the wake. The Y-Z Reynolds shear stress remains low compared to the others. It is also remarkable to see a large extension of the mixing zones between the low and the high turbulent cases for the three Reynolds shear stress components.

3.2 Investigation on the replenishment mechanisms

In order to understand what phenomenon induce a faster wake recovery in presence of inflow turbulence, the maps of the transport terms are presented in appendix D, figures D1a to D4b. The contribution of mean flow, appears to be about 2 times

https://doi.org/10.5194/wes-2026-160
Preprint. Discussion started: 14 September 2026

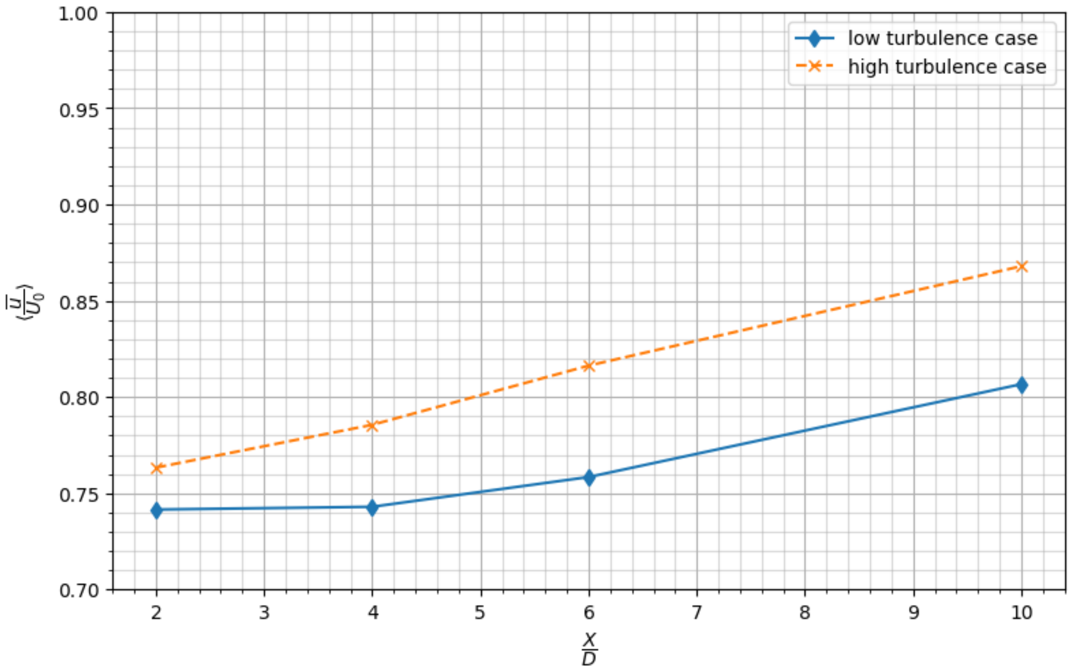

Figure 8. Mean velocity in the reference surface as a function of downstream distance.

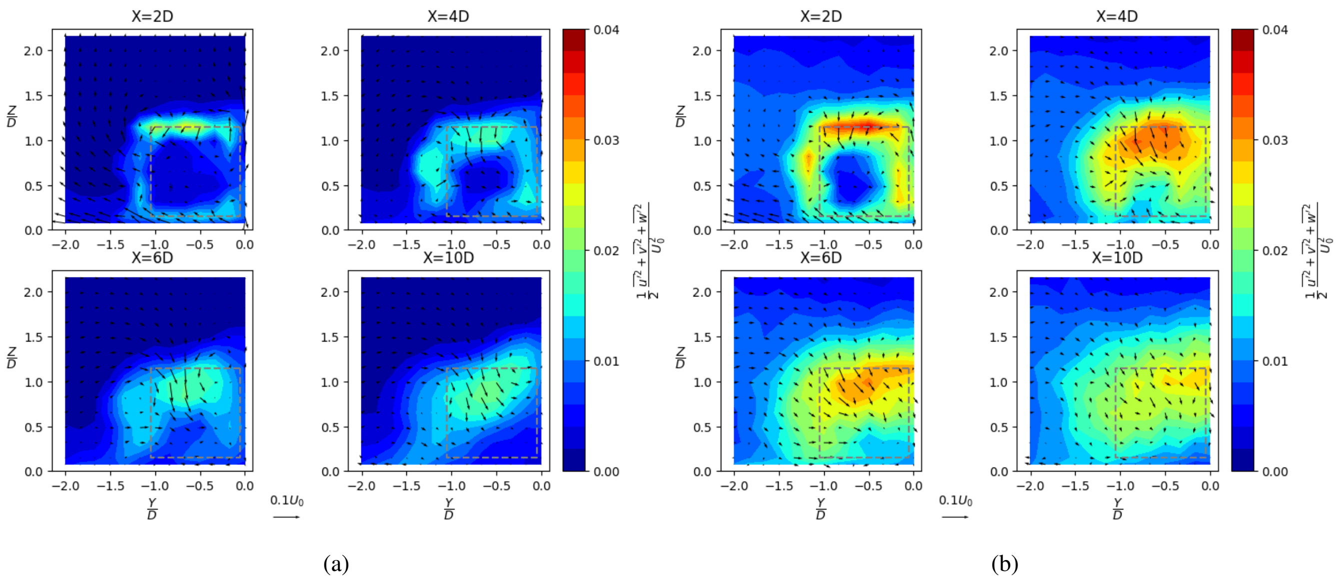

Figure 9. Turbulent kinetic energy color-map for the low turbulence case (a) and high turbulence case (b). The colors represent the axial velocity, the arrows represent the cross-stream velocity. The dashed gray lines represent the rotors.

https://doi.org/10.5194/wes-2026-160
Preprint. Discussion started: 14 September 2026

eawe european academy of wind energy
Open Access WIND ENERGY SCIENCE DISCUSSIONS

higher than the contribution of turbulent flow. The areas where the contribution of turbulent transport is high are located at the core of the wake. The areas where the contribution of the mean flow is high tend to be located towards the edges of the wake. They are also concomitant with high transverse speeds. In both case, the vertical transport seems to be the major contributor. The dissipation of the mean horizontal and vertical transport terms is higher for the high turbulence case compare to the low one.

Therefore, the maps of the mean vertical transport terms in the low and high turbulence case are shown in figure 10. The cross-stream velocities are represented by the arrows. Especially in the low turbulence case, the vertical transport by the mean flow seems to be due to a pair of stationary longitudinal vortices located in the two upper corners of the wake. This phenomenon drives the wake recovery and has already been observed in the literature for VAWTs (Rolin and Porté-Agel, 2018; Talamalek et al., 2024). The vertical transport seems to settle and disappear sooner in the high turbulence case.

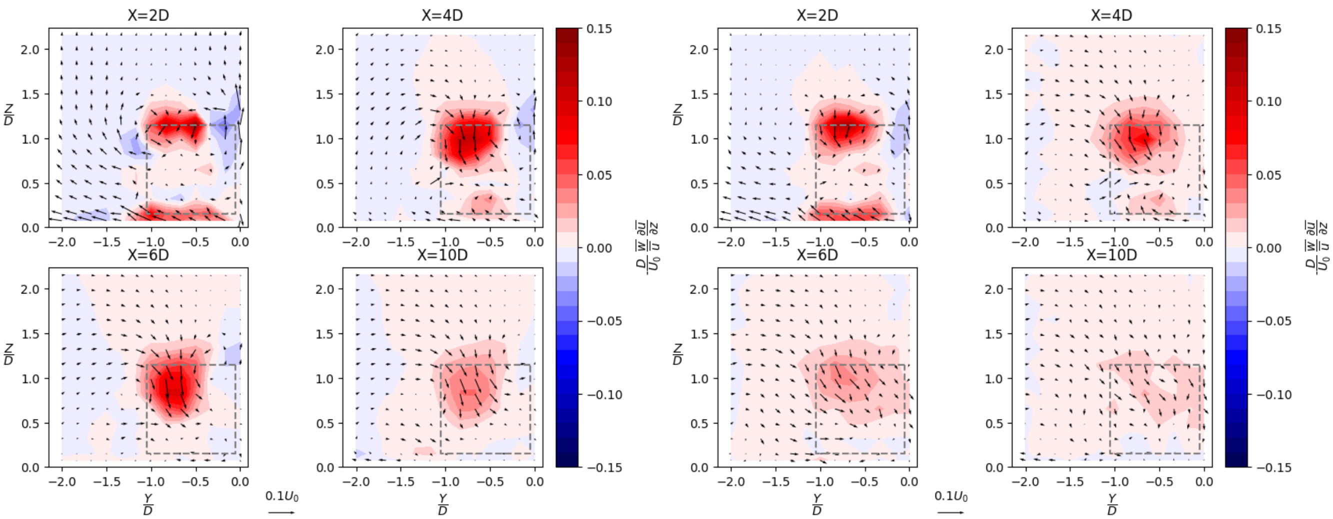

(a) (b)

Figure 10. Turbulent kinetic energy color-map for the low turbulence case (a) and high turbulence case (b). The colors represent the axial velocity, the arrows represent the cross-stream velocity. The dashed gray lines represent the rotors.

In order to compare the wake replenishment mechanism of the two flow cases, the average of all the transport terms over the reference surface is plotted figure 11. In the low turbulence case, the contribution of the mean flow along Y is negative for $X/D = 2$, then becomes positive in $X/D = 4$. The contribution of the mean flow along Z is positive for the near wake, but really settles in at $X/D = 4$. This corresponds with the observation of the pair of stationary vortices seen in the maps at $X/D = 4$, which are not yet fully developped at $X/D = 2$. The contribution of the mean flow remains at a maximum until $X/D = 6$, then starts to decrease between $X/D = 6$ and $X/D = 10$. The contribution of the turbulent flow is smaller than the contribution of the mean flow. It varies little and reaches a maximum at $X/D = 4$. All these observations are consistent with previous results (Talamalek et al., 2024; Bachant and Wosnik, 2015) who carried out similar studies in low turbulence cases. For the high turbulence case, the contributions of the mean flow are already at their maximum at $X/D = 2$. They remain at

https://doi.org/10.5194/wes-2026-160
Preprint. Discussion started: 14 September 2026

their maximum until $X/D = 4$ and then start to decrease. The stationary phenomena contributing to the vertical transport starts and decreases closer to the wind turbine than in the low turbulence case. The contribution of the turbulent flow is higher than in the low turbulence case, but remains significantly lower than the contribution of the mean flow.

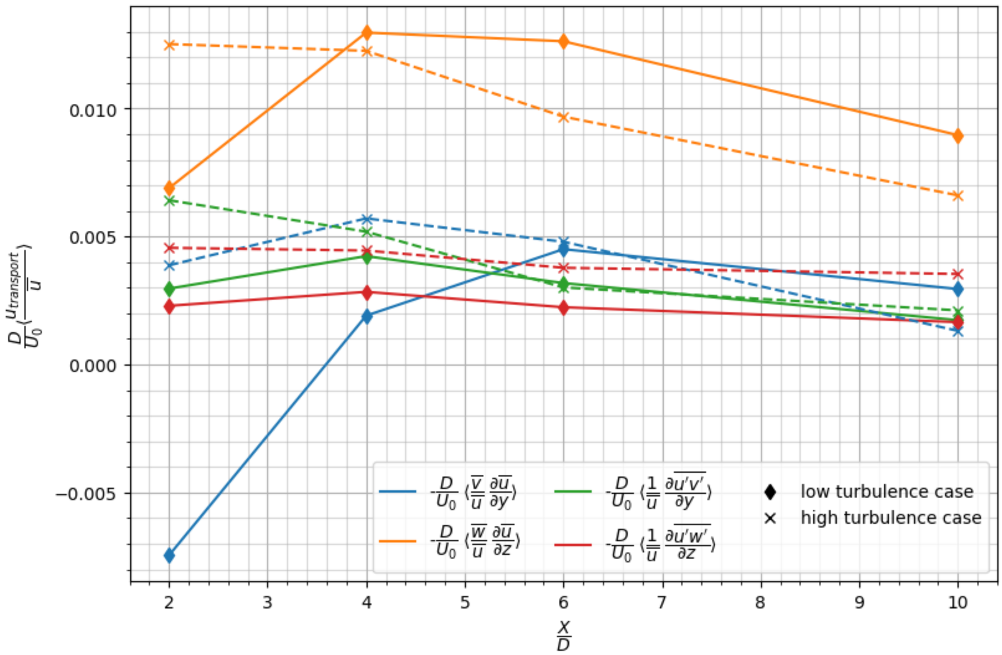

Figure 11. Contribution of the momentum transport terms averaged over the reference surface, as a function of the down-stream distance.

The sum of the contributions of the mean and turbulent flow for the two cases studied are presented in figure 12. For $X/D < 6$ the momentum transport is higher in the high turbulence case, which explains the higher recovery speed. Further downstream, the transport is similar in both cases, and so the two wakes recover at the same speed, as observed in figure 8.

3.3 Link between the wake replenishment mechanisms and the upstream turbulence

The results presented in section 3.2 shows that the major contributor for the stream-wise momentum transport is the vertical advection $-\frac{\overline{w}}{\overline{u}}\frac{\partial \overline{u}}{\partial z}$. The figure 11 shows that this term reaches a maximum before $X/D = 6$ and then decreases. The vertical advection is the multiplication of the normalized vertical velocity $-\frac{\overline{w}}{\overline{u}}$ and the vertical gradient of stream-wise velocity $\frac{\partial \overline{u}}{\partial z}$. At $X/D = 2$, the vertical advection is significantly higher in the high turbulence case. However, as the velocity deficit are similar, there is no significant difference in the vertical gradient of stream-wise velocity. The difference in vertical advection is mostly due to the normalized vertical velocity. The average normalized vertical velocity over the reference surface is plotted figure 13. The downward velocity is overall higher for the high turbulence case. The downward velocity highly increases up to $X/D = 6$ and slightly decreases from $X/D = 6$. After $X/D = 6$, the high downward velocity $-\frac{\overline{w}}{\overline{u}}$ is compensated by the wake

https://doi.org/10.5194/wes-2026-160
Preprint. Discussion started: 14 September 2026

WIND ENERGY SCIENCE DISCUSSIONS

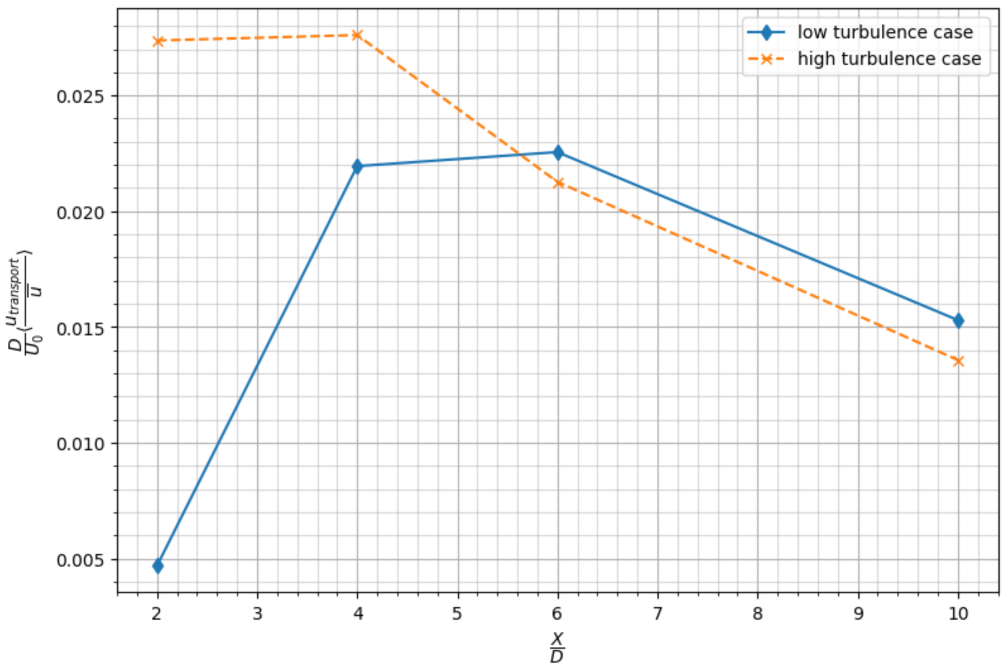

Figure 12. Sum of the contributions of the momentum transport terms averaged over the reference surface, as a function of the down-stream distance.

resorption which causes a decrease of the velocity gradient $\frac{\partial \overline{u}}{\partial z}$. This explain the behaviour of the vertical advection displayed in figure 11.

The higher downward velocity in the high turbulence case has an important effect on the vertical advection. In order to study the onset of this downward velocity, the method applied in equation 7, presented in appendix A can be applied on the Reynolds equation on Z axis. It results in equation 8.

$$\frac{\partial \overline{w}}{\partial x} = \frac{1}{\overline{u}}\left[-\overline{v}\frac{\partial \overline{w}}{\partial y} - \overline{w}\frac{\partial \overline{w}}{\partial z} - g - \frac{1}{\rho}\frac{\partial \overline{p}}{\partial z} - \frac{\partial \overline{w'u'}}{\partial x} - \frac{\partial \overline{w'v'}}{\partial y} - \frac{\partial \overline{w'^2}}{\partial z}\right] + \frac{1}{\overline{u}}\left[\nu\left(\frac{\partial^2 \overline{w}}{\partial x^2} + \frac{\partial^2 \overline{w}}{\partial y^2} + \frac{\partial^2 \overline{w}}{\partial z^2}\right)\right] \quad (8)$$

The viscosity transport term $\frac{\nu}{\overline{u}}\left(\frac{\partial^2 \overline{w}}{\partial x^2} + \frac{\partial^2 \overline{w}}{\partial y^2} + \frac{\partial^2 \overline{w}}{\partial z^2}\right)$ remains negligible as the Reynolds number is high. The pressure gradient $-\frac{1}{\overline{u}\rho}\frac{\partial \overline{p}}{\partial z}$ is not measured here. $g = -9.81 m/s^2$ is the gravity acceleration. The term $-\frac{1}{\overline{u}}\frac{\partial \overline{w'u'}}{\partial x}$ isn't calculated because of the large distances between the measurement points along X. The terms $-\frac{1}{\overline{u}}\frac{\partial \overline{w'v'}}{\partial y}$ and $-\frac{1}{\overline{u}}\frac{\partial \overline{w'^2}}{\partial z}$ are the horizontal and vertical turbulent transport terms.

In the aim of understanding the downward velocity's establishment, figure 14 shows the different terms involved in the vertical cross-stream momentum. In both case, the major contributor is the vertical turbulent transport term $-\frac{\partial \overline{w'^2}}{\partial z}$. The higher value of this term in the high turbulence case is identified to be responsible for the earlier onset of the vertical advection. The

https://doi.org/10.5194/wes-2026-160
Preprint. Discussion started: 14 September 2026

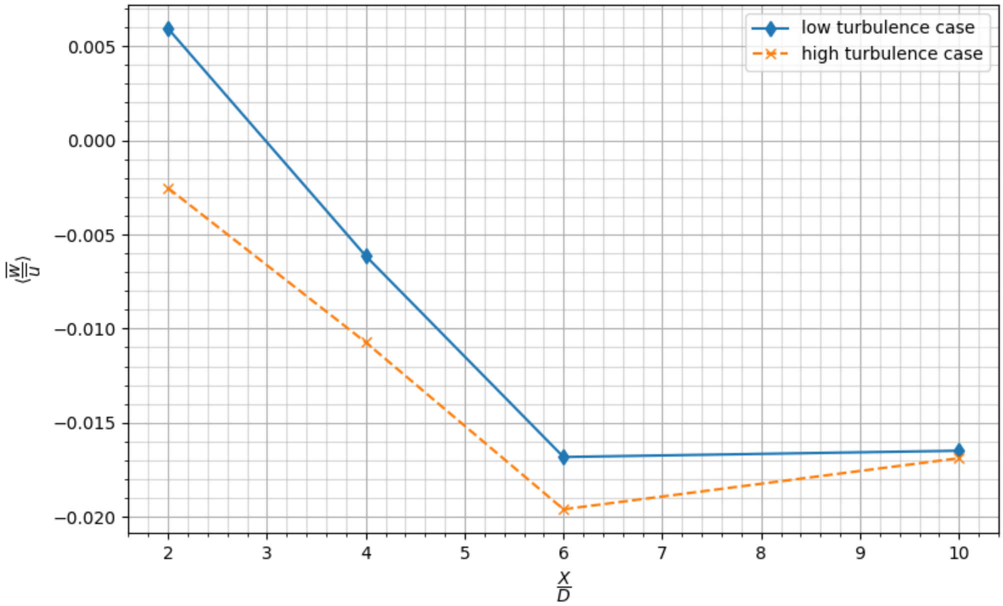

Figure 13. Mean normalized vertical velocity in the reference surface as a function of downstream distance.

difference in the spatial repartition of the vertical turbulence component in the wake induced by the inflow turbulence intensity can be observed in figure C3a and C3b of appendix C.

4 Discussion of the wake replenishment mechanisms identified

Figure 15 presents the contributions of the stream-wise momentum transport terms in the form of a bar graph. It compares the contribution of mean and turbulent flow to the wake resorption. In this way, it helps to understand which physical phenomenon is responsible for the faster wake resorption in the high turbulence case. In the scientific literature, the added turbulence in the wake is often presented as the phenomenon responsible for the rapid resorption of the wake (van der Deijl et al., 2024; Chu and Chiang, 2014; Peng and Lam, 2016; Dabiri, 2011). This added turbulence is clearly observed here (Figure 9b) and is indeed at the origin of an increase in the contribution of turbulence to the stream-wise momentum transport. However, it's major effect seems to be found in the vertical cross-stream momentum transport. By increasing the vertical momentum transport, the inflow turbulence helps onsetting the vertical advection in the wake. Figure 15 shows that it is the early onset of this vertical advection in the wake that mostly contribute to the increase in momentum transport between $X/D = 2$ and $X/D = 4$. At $X/D = 4$, the contribution of the vertical advection in the stream-wise momentum transport is equivalent to the low turbulence case. Further downstream, the contribution of these structures decreases, and becomes slightly lower than in the low turbulence case. The contribution of the added turbulence is then just enough to compensate for this deficit. Therefore, the wakes recover at the same

https://doi.org/10.5194/wes-2026-160
Preprint. Discussion started: 14 September 2026

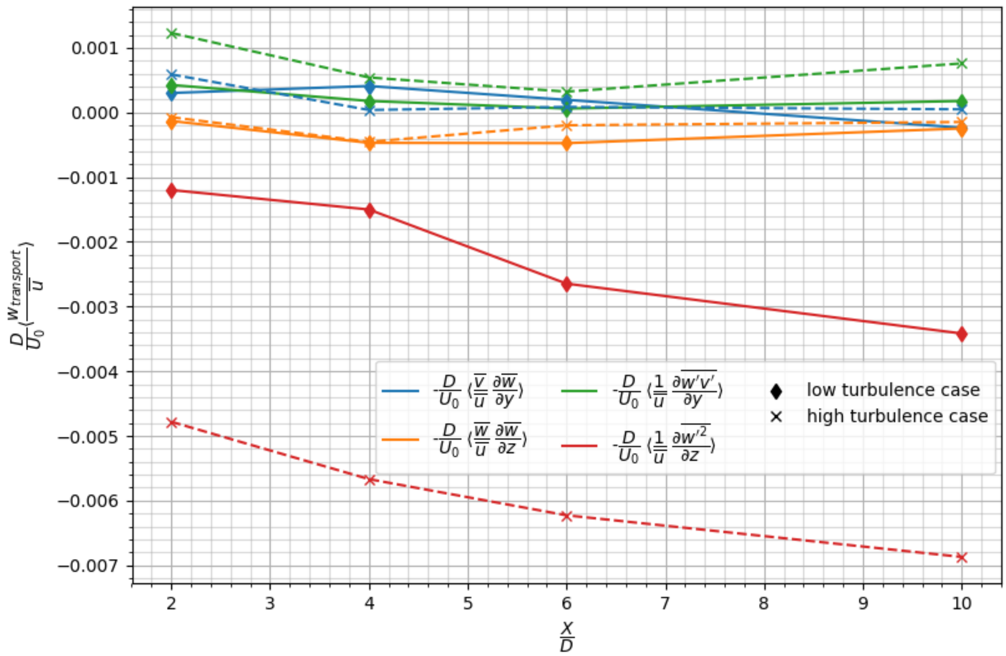

Figure 14. Contribution of the vertical cross-stream momentum transport terms averaged over the reference surface, as a function of the down-stream distance.

speed, with an offset retain for the high turbulence case. As a result, Figure 8 shows that at $X/D = 10$, the average velocity on the reference surface is $< U >= 0.8U_0$ for the low turbulence case and $< U >= 0.86U_0$ for the high turbulence case.

For both the stream-wise velocity and the cross-stream velocities, not all the terms contributing to the momentum transport are calculated. This is due to the large distances between measurement planes in X axis, and to the missing pressure measurement. Other experimental campaigns with PIV and pressure measurement, or a computational fluid dynamic study could give access to these missing terms. Having these terms is necessary to close the momentum budget, which is important for the cross-stream velocities where the pressure gradient have a strong impact.

As $\frac{1}{u}$ is involved in the momentum transport budget equation, the inflow velocity profile can affect the transport terms in the vertical direction. It underline the importance of accurately reproducing the on site conditions in order to obtain consistent results.

Especially in the low turbulence case, the horizontal advection counterbalances the vertical advection in the very near wake, resulting in no replenishment close to the wind turbine. Therefore the horizontal cross-stream momentum transport terms have been studied in order to understand the differences in horizontal advection between the low and high turbulence case. No explanation has been found in the transport terms calculated in this work.

The reference surface for averaging the transport terms has been found to have an impact on the results. Here, the surface has been chosen as it contains all the wake and all the area of high momentum transport. However, all the conclusions remain the

https://doi.org/10.5194/wes-2026-160
Preprint. Discussion started: 14 September 2026

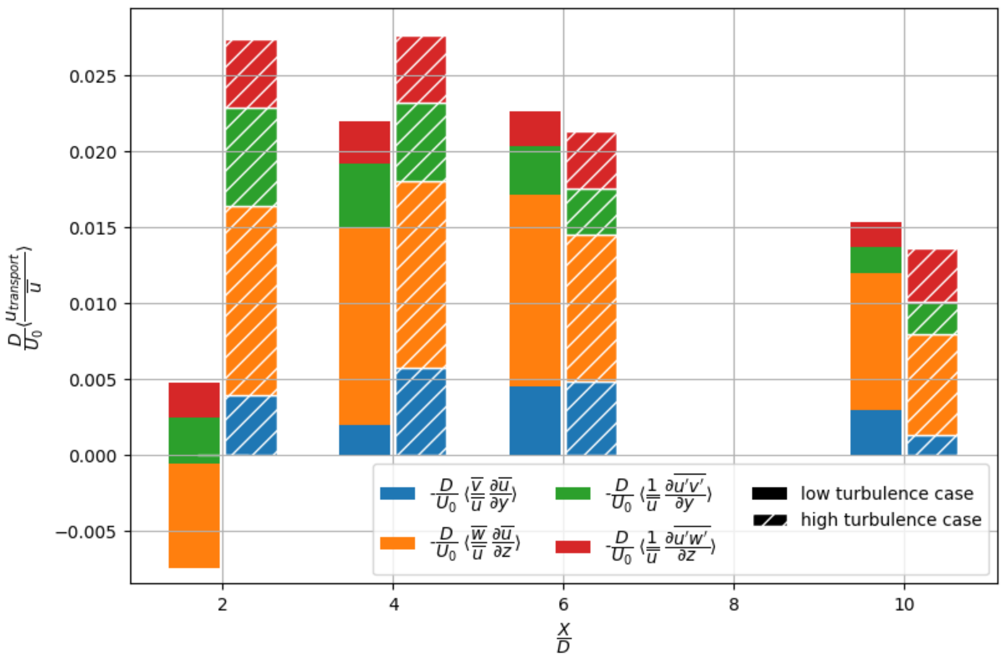

Figure 15. Bar plot of the contributions of the momentum transport terms averaged over the reference surface for all the measurement planes.

same regardless of the reference surfaces investigated.

5 Conclusions

In this work, the wake of a twin rotor vertical axis wind turbine has been characterized by 3 components Laser Doppler Velocimetry in order to investigate how the inflow turbulence affect the wake replenishment mechanisms. The experiment was performed with inflow conditions that are representative of an offshore atmospheric boundary layer velocity profile, for two turbulence intensity levels. Measurements were located in a uniform grid of dimension $2D \times 2H$, in 4 cross-stream planes at downstream distances from $2D$ to $10D$.

In accordance with the results from the literature, the wake recovers faster in the high turbulence case. This confirms that the inflow turbulence level is a key parameter in order to represent a realistic wake in small scale test. For each case, the different terms contributing to the momentum transports were calculated and averaged over a reference surface. The vertical advection has been found to be the major contributor to the momentum transport for both low and high turbulence case. In contrast with the classical assumption that the turbulent mixing is responsible for the faster wake resorption in the high turbulence case, it is the earlier onset of the vertical advection that explain the faster wake recovery. The onset of the vertical advection is seemingly due to the turbulent transport of cross-stream vertical momentum, which is enhanced by the added turbulence.

https://doi.org/10.5194/wes-2026-160
Preprint. Discussion started: 14 September 2026

This explanation offers a better understanding of the VAWT wake dynamics. This result could be compared to numerical studies in order to verify that numerical model such as LES correctly take into account the inflow turbulence on the wake
290 dynamics. It could also help design efficient farms layout.

Data availability. on demand

Appendix A: Mean kinetic budget equation

Starting from the Reynolds averaged Navier-Stokes equation projected on x-axis:

$$\frac{\partial \overline{u}}{\partial t} + \overline{u}\frac{\partial \overline{u}}{\partial x} + \overline{v}\frac{\partial \overline{u}}{\partial y} + \overline{w}\frac{\partial \overline{u}}{\partial z} = -g_x - \frac{1}{\rho}\frac{\partial \overline{p}}{\partial x} - \frac{\partial \overline{u'^2}}{\partial x} - \frac{\partial \overline{u'v'}}{\partial y} - \frac{\partial \overline{u'w'}}{\partial z} + \nu\left(\frac{\partial^2 \overline{u}}{\partial x^2} + \frac{\partial^2 \overline{u}}{\partial y^2} + \frac{\partial^2 \overline{u}}{\partial z^2}\right)$$

295 The problem is stationary, then the time derivative is equal to 0. The projection of $\boldsymbol{g}$ on x-axis is equal to zeros. Therefore, mooving $\overline{v}\frac{\partial \overline{u}}{\partial y} + \overline{w}\frac{\partial \overline{u}}{\partial z}$ to the right hand side of the equation :

$$\overline{u}\frac{\partial \overline{u}}{\partial x} = \overline{v}\frac{\partial \overline{u}}{\partial y} + \overline{w}\frac{\partial \overline{u}}{\partial z} - \frac{1}{\rho}\frac{\partial \overline{p}}{\partial x} - \frac{\partial \overline{u'^2}}{\partial x} - \frac{\partial \overline{u'v'}}{\partial y} - \frac{\partial \overline{u'w'}}{\partial z} + \nu\left(\frac{\partial^2 \overline{u}}{\partial x^2} + \frac{\partial^2 \overline{u}}{\partial y^2} + \frac{\partial^2 \overline{u}}{\partial z^2}\right)$$

Dividing by $\overline{u}$:

$$\frac{\partial \overline{u}}{\partial x} = \frac{1}{\overline{u}}\left[\overline{v}\frac{\partial \overline{u}}{\partial y} + \overline{w}\frac{\partial \overline{u}}{\partial z} - \frac{1}{\rho}\frac{\partial \overline{p}}{\partial x} - \frac{\partial \overline{u'^2}}{\partial x} - \frac{\partial \overline{u'v'}}{\partial y} - \frac{\partial \overline{u'w'}}{\partial z}\right] + \frac{1}{\overline{u}}\left[\nu\left(\frac{\partial^2 \overline{u}}{\partial x^2} + \frac{\partial^2 \overline{u}}{\partial y^2} + \frac{\partial^2 \overline{u}}{\partial z^2}\right)\right]$$

300 Appendix B: Comparison with PIV measurements

PIV measurements were performed in the middle X-Z plane of one rotor. Comparison are possible at the intersection of the PIV plane and the LDV plane at $X/D = 2$ and $X/D = 4$. Figure B1 shows the longitudinal velocity profiles at these location obtained by PIV and LDV with interpolation and coincidence method. Both LDV methods give consistent result with the PIV measurements.

305 Figure B2 shows the X-Z Reynolds sheared stress and Z Reynolds normal stress. The classical underestimation of $\overline{u'w'}$ and the overestimation of $\overline{w'^2}$ (Boutier, 2012) are observed in the LDV interpolation data. The underestimation of $\overline{u'w'}$ is not observed in the coincidence method. The overestimation of $\overline{w'^2}$ is significantly reduced by the coincidence method.

https://doi.org/10.5194/wes-2026-160
Preprint. Discussion started: 14 September 2026

Open Access
WIND ENERGY SCIENCE
DISCUSSIONS

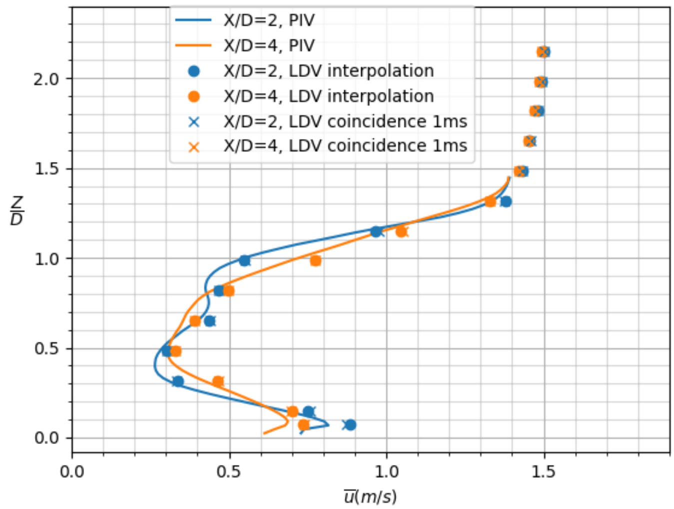

Figure B1. Vertical velocity profiles obtained with PIV and LDV measurement in the middle plane of one rotor, at $X/D = 2$ and $X/D = 2$.

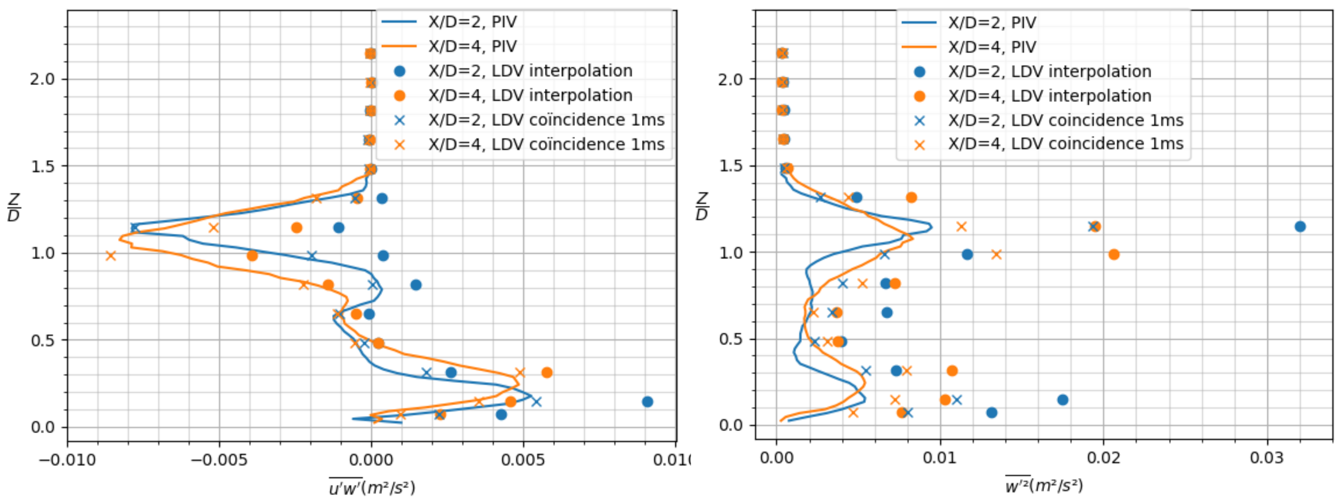

Figure B2. Vertical X-Z Reynolds sheared stress and Z Reynolds normal stress profiles obtained with PIV and LDV measurement in the middle plane of one rotor, at $X/D = 2$ and $X/D = 2$.

Appendix C: Reynolds tensor color maps

The areas of high Reynolds normal stress and the distribution of X-Y Reynolds shear stress in the turbine wake are highlighted in figures C1 to C6.

https://doi.org/10.5194/wes-2026-160
Preprint. Discussion started: 14 September 2026

WIND ENERGY SCIENCE DISCUSSIONS

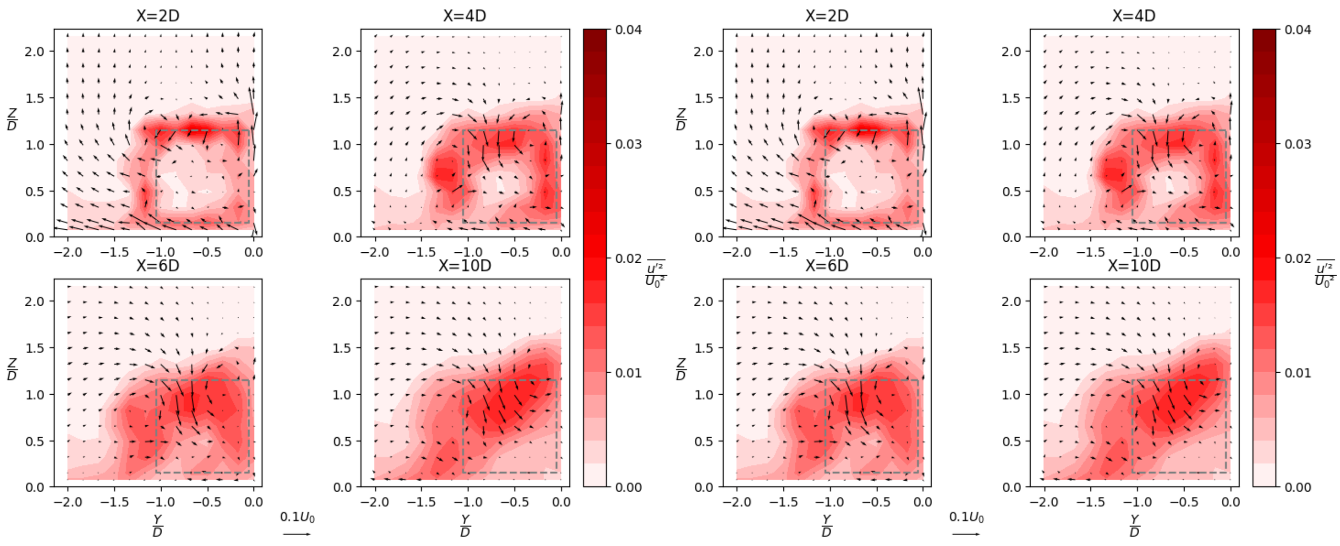

(a) (b)

Figure C1. X Reynolds normal stress for the low turbulence case (a) and high turbulence case (b).

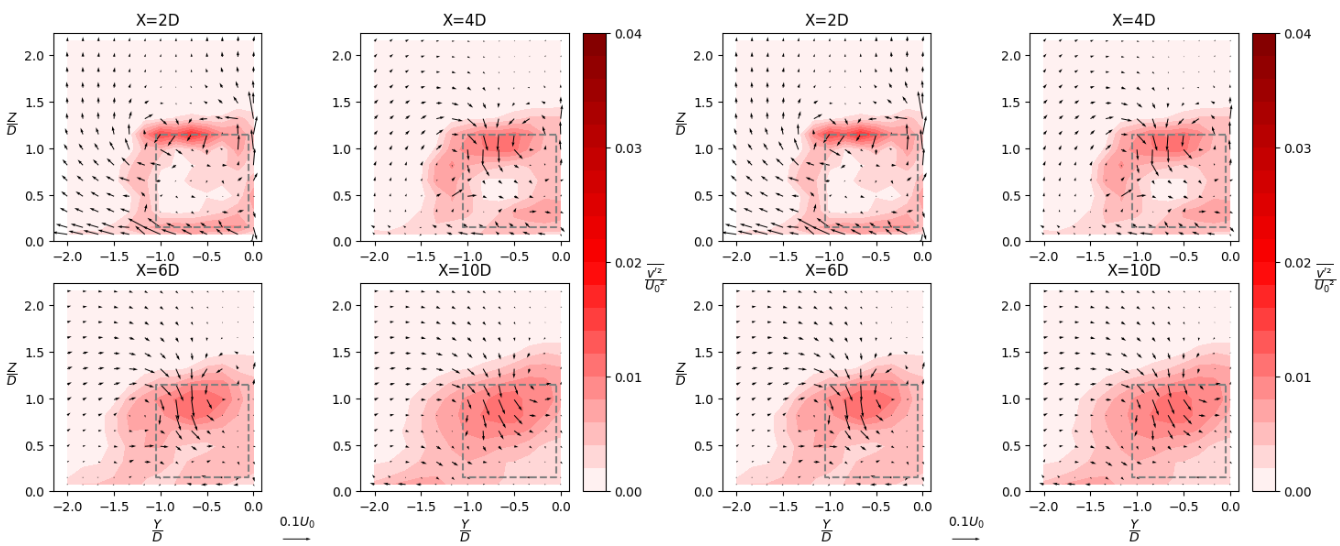

(a) (b)

Figure C2. Y Reynolds normal stress for the low turbulence case (a) and high turbulence case (b).

https://doi.org/10.5194/wes-2026-160
Preprint. Discussion started: 14 September 2026

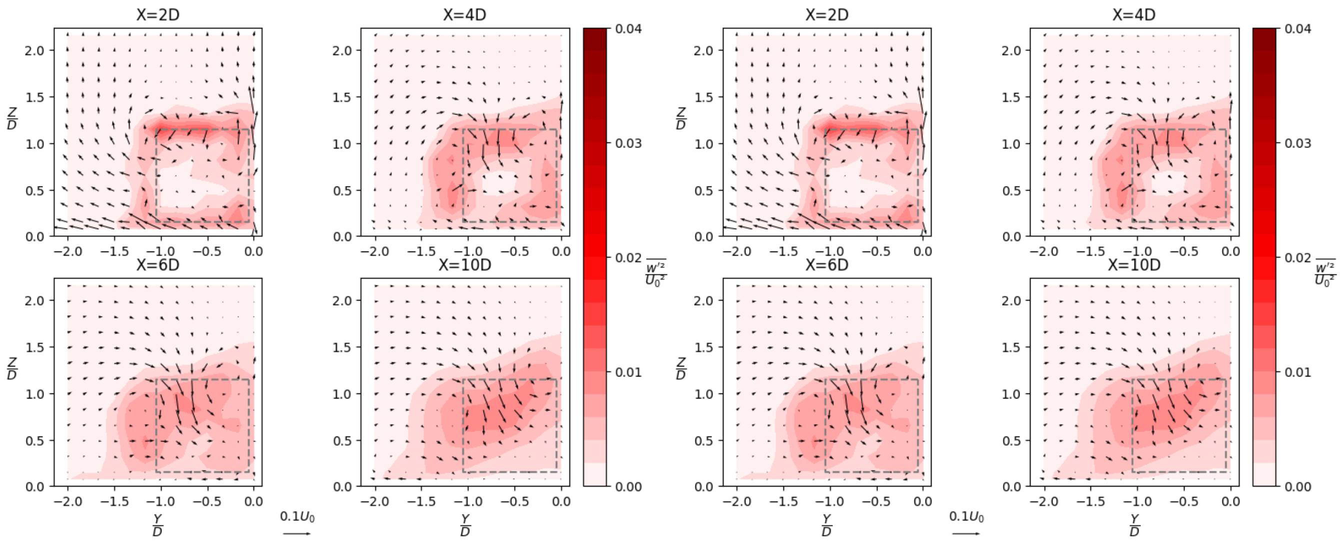

(a) (b)

Figure C3. Z Reynolds normal stress for the low turbulence case (a) and high turbulence case (b).

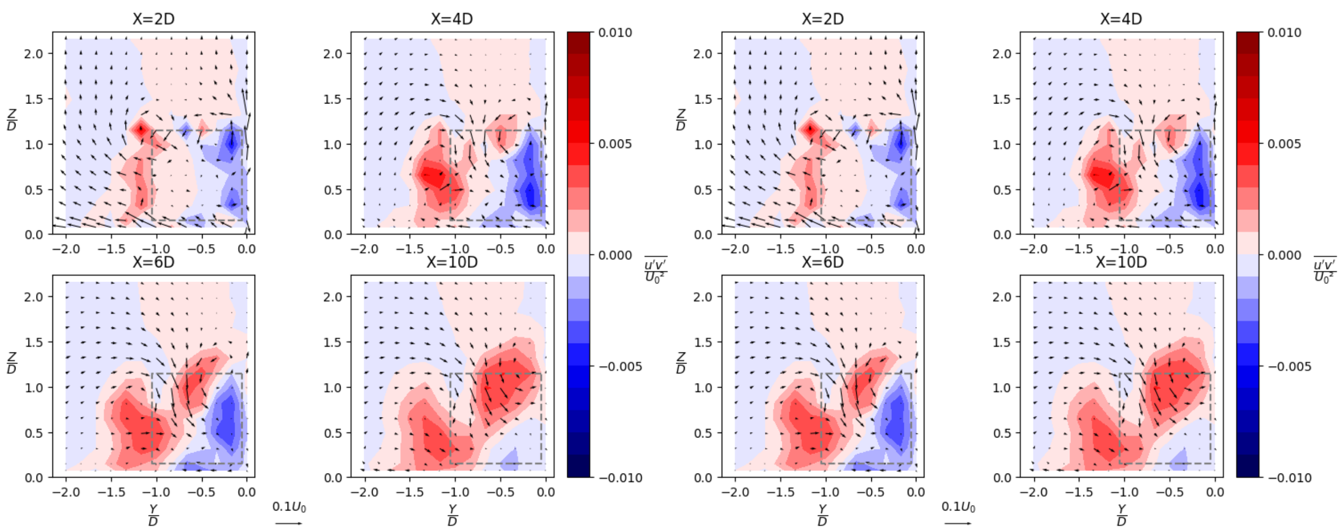

(a) (b)

Figure C4. X-Y Reynolds shear stress for the low turbulence case (a) and high turbulence case (b).

https://doi.org/10.5194/wes-2026-160
Preprint. Discussion started: 14 September 2026

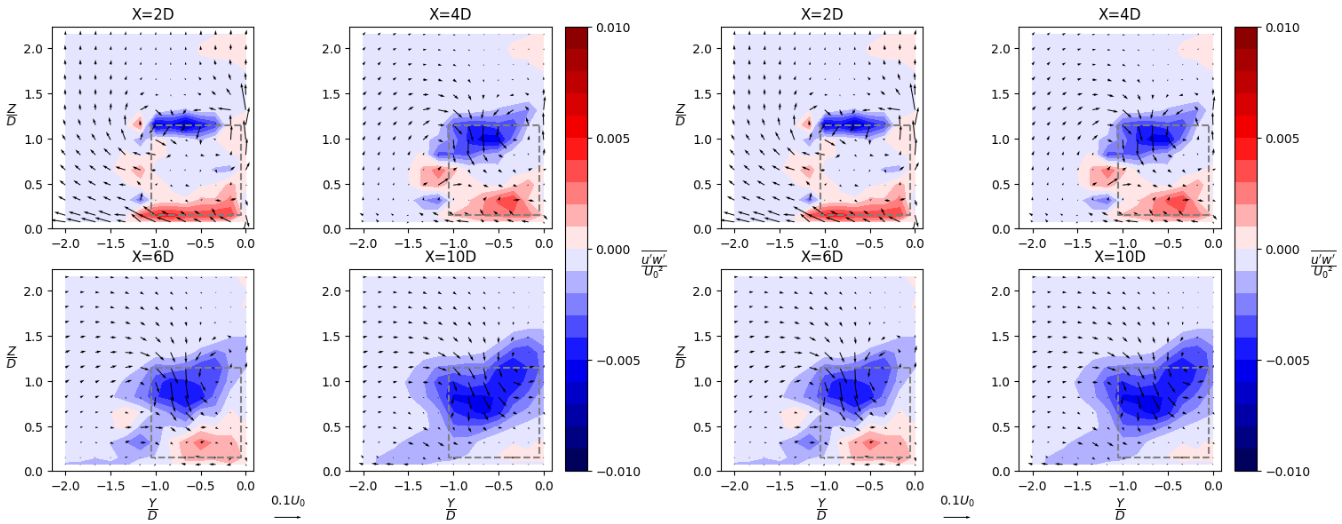

(a) (b)

Figure C5. X-Z Reynolds shear stress for the low turbulence case (a) and high turbulence case (b).

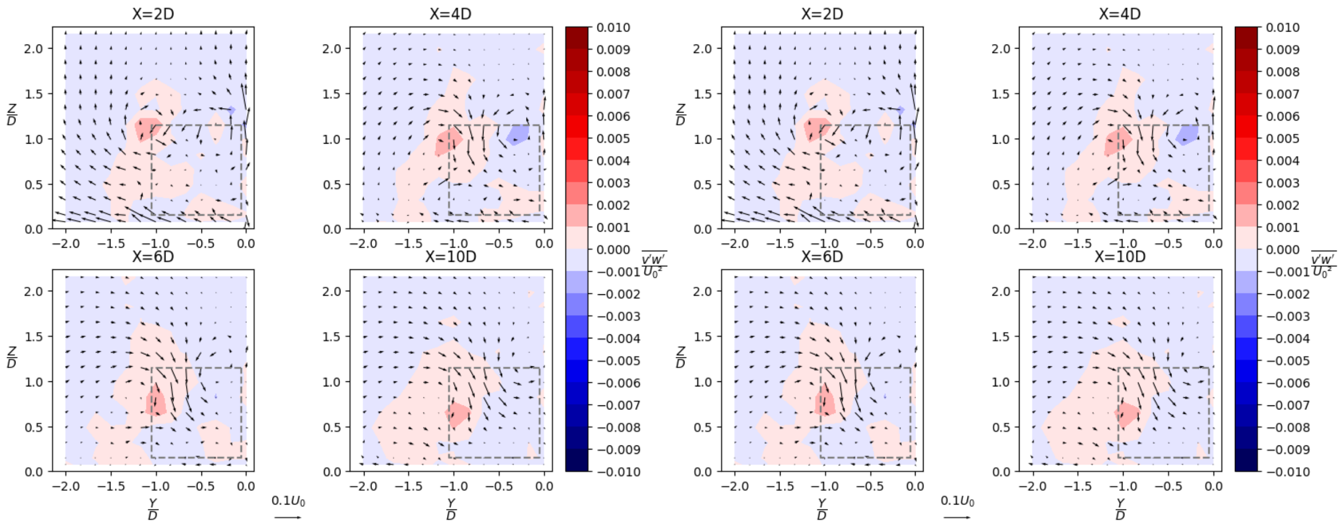

(a) (b)

Figure C6. Y-Z Reynolds shear stress for the low turbulence case (a) and high turbulence case (b).

https://doi.org/10.5194/wes-2026-160
Preprint. Discussion started: 14 September 2026

Appendix D: Momentum transport

The maps of the transport terms (mean and turbulent flow horizontal and vertical transport terms) are presented figures D1 to D4.

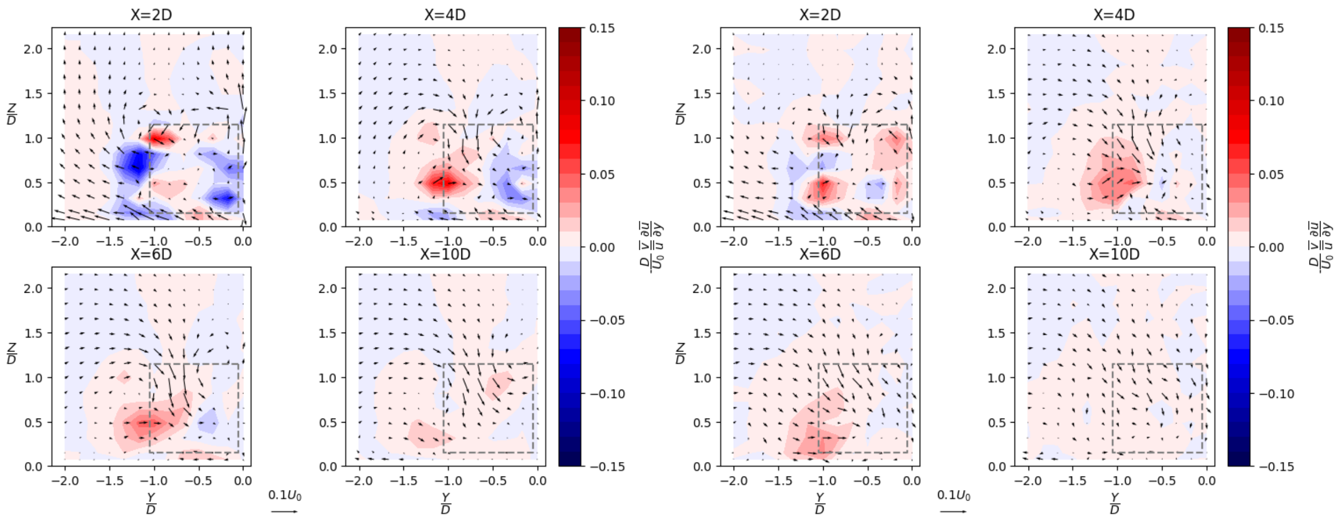

(a) (b)

Figure D1. Mean flow horizontal transport for the low turbulence case (a) and high turbulence case (b).

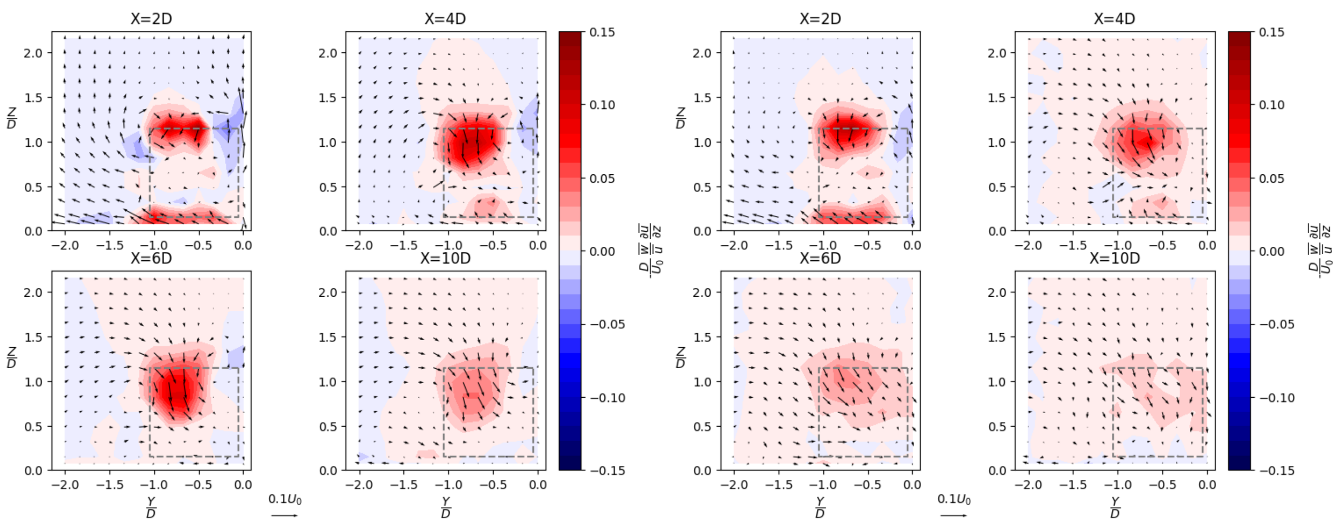

(a) (b)

Figure D2. Mean flow vertical transport for the low turbulence case (a) and high turbulence case (b).

https://doi.org/10.5194/wes-2026-160
Preprint. Discussion started: 14 September 2026

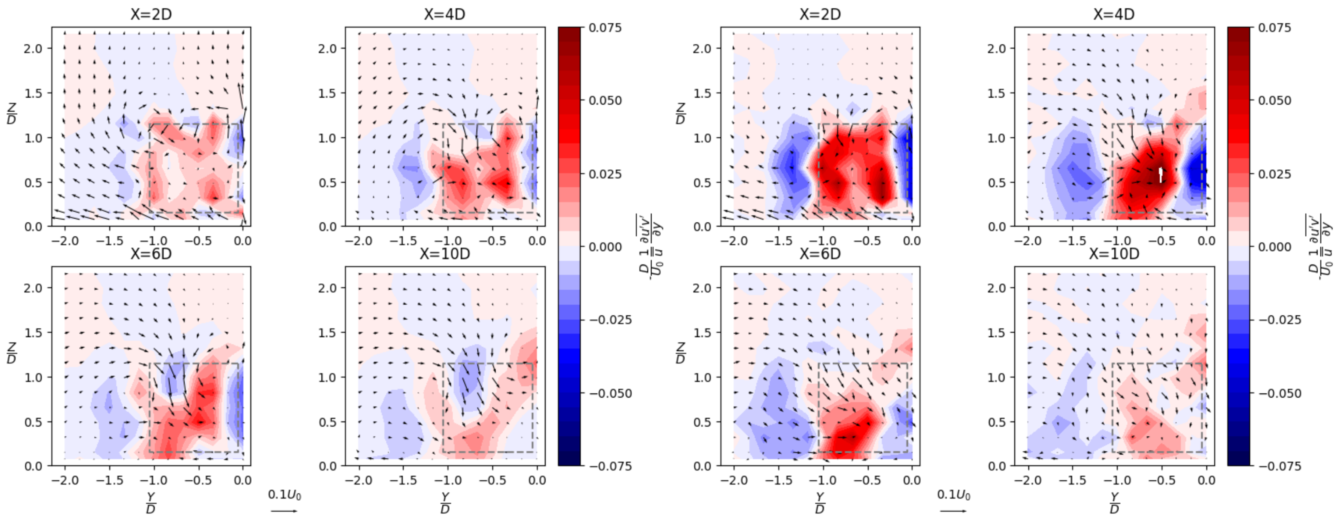

(a) (b)

Figure D3. Turbulent flow horizontal transport for the low turbulence case (a) and high turbulence case (b).

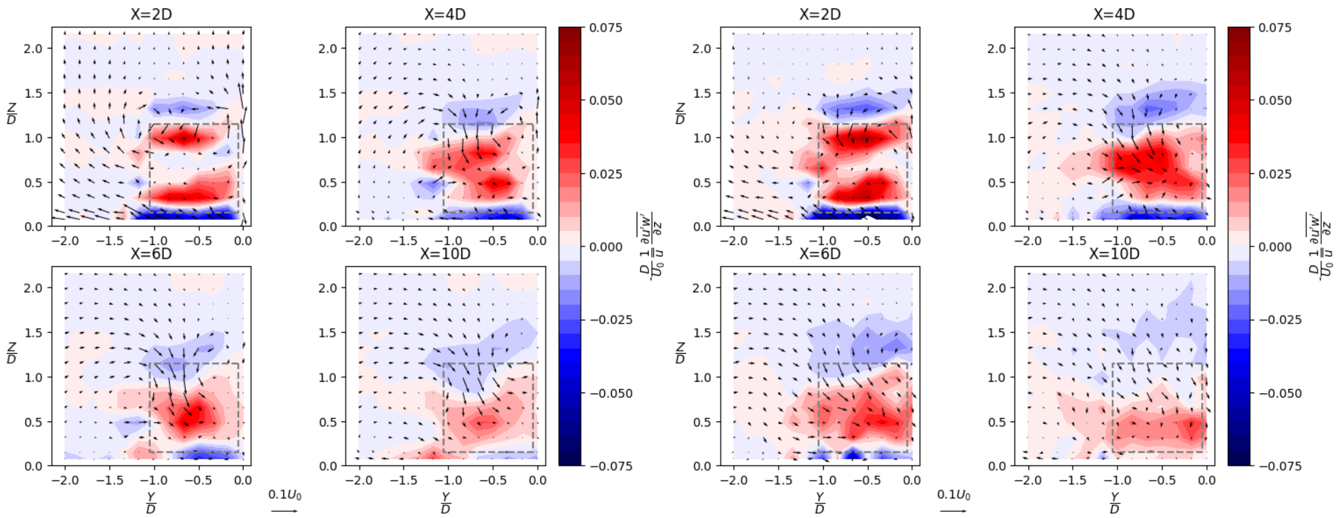

(a) (b)

Figure D4. Turbulent flow vertical transport for the low turbulence case (a) and high turbulence case (b).

Author contributions. – Funding : Matthieu Minguez.

– Conceptualization : Simon Querat.

– Methodology : Simon Querat, Benoît Augier, Martin Träsch, Gregory Grermain, Antoine Delon, Matthieu Minguez, Stephane Barre.

– Data curation : Simon Querat, Gregory Grermain, Antoine Delon.

https://doi.org/10.5194/wes-2026-160
Preprint. Discussion started: 14 September 2026

- Formal analysis : Simon Querat, Gregory Grermain, Benoît Augier, Martin Träsch.
- Writing (original draft preparation) : Simon Querat.
- Writing (review and editing) : Simon Querat, Benoît Augier, Martin Träsch, Gregory Grermain, Antoine Delon, Matthieu Minguez, Stephane Barre.

Competing interests. Matthieu Minguez is the founder of the Bluetwin company which provide the wind turbine design studied in this work.

Acknowledgements. This work benefited from France 2030 state financing managed by the French Agency for Ecological Transition, under the DEMO-TASE Floatwin project.
This work benefited from BPI France financing under the Deeptech development support.

https://doi.org/10.5194/wes-2026-160
Preprint. Discussion started: 14 September 2026

References

Achard, J.-L., Maurice, G., Balarac, G., and Barre, S.: Floating vertical axis wind turbine—OWLWIND project, in: 2017 International Conference on ENERGY and ENVIRONMENT (CIEM), pp. 216–220, IEEE, 2017.

Bachant, P. and Wosnik, M.: Characterising the near-wake of a cross-flow turbine, Journal of turbulence, 16, 392–410, 2015.

Boudreau, M. and Dumas, G.: Comparison of the wake recovery of the axial-flow and cross-flow turbine concepts, Journal of Wind Engineering and Industrial Aerodynamics, 165, 137–152, 2017.

Boutier, A.: Laser velocimetry in fluid mechanics, John Wiley & Sons, 2012.

Bromm, M., Rott, A., Beck, H., Vollmer, L., Steinfeld, G., and Kühn, M.: Field investigation on the influence of yaw misalignment on the propagation of wind turbine wakes, Wind Energy, 21, 1011–1028, 2018.

Brown, K., Houck, D., Maniaci, D., Westergaard, C., and Kelley, C.: Accelerated wind-turbine wake recovery through actuation of the tip-vortex instability, AIAA Journal, 60, 3298–3310, 2022.

Chu, C.-R. and Chiang, P.-H.: Turbulence effects on the wake flow and power production of a horizontal-axis wind turbine, Journal of Wind Engineering and Industrial Aerodynamics, 124, 82–89, 2014.

Dabiri, J. O.: Potential order-of-magnitude enhancement of wind farm power density via counter-rotating vertical-axis wind turbine arrays, Journal of renewable and sustainable energy, 3, 2011.

Magnier, M.: Étude expérimentale de l'effet des courants de marée et de la houle sur la dynamique tourbillonnaire d'une variation bathymétrique et sur le comportement d'une hydrolienne, Ph.D. thesis, Université de lille, 2023.

Matoug, C., Augier, B., Paillard, B., Maurice, G., Sicot, C., and Barre, S.: An hybrid approach for the comparison of VAWT and HAWT performances for floating offshore wind turbines, in: Journal of Physics: Conference Series, vol. 1618, p. 032026, IOP Publishing, 2020.

Moreau, M., Germain, G., and Maurice, G.: Experimental performance and wake study of a ducted twin vertical axis turbine in ebb and flood tide currents at a 1/20th scale, Renewable Energy, 214, 318–333, 2023.

Ouro, P., Runge, S., Luo, Q., and Stoesser, T.: Three-dimensionality of the wake recovery behind a vertical axis turbine, Renewable Energy, 133, 1066–1077, 2019.

Peng, H. and Lam, H.: Turbulence effects on the wake characteristics and aerodynamic performance of a straight-bladed vertical axis wind turbine by wind tunnel tests and large eddy simulations, Energy, 109, 557–568, 2016.

Rolin, V. F. and Porté-Agel, F.: Experimental investigation of vertical-axis wind-turbine wakes in boundary layer flow, Renewable energy, 118, 1–13, 2018.

Talamalek, A., Runacres, M. C., and De Troyer, T.: Experimental investigation of the wake replenishment mechanisms of paired counter-rotating vertical-axis wind turbines, Journal of Wind Engineering and Industrial Aerodynamics, 252, 105 830, 2024.

Talamalek, A., Runacres, M. C., and De Troyer, T.: Effect of Free-Stream Turbulence on the Power Performance and Wake Characteristics of Paired Counter-Rotating Vertical-Axis Wind Turbines, Wind Energy, 28, e2968, 2025.

Thiébaut, M., Delbos, F., Benzo, C., Mahe, L., and Guinot, F.: Enhancing turbulent fluctuation measurement with tailored wind lidar profilers, Wind Energy Science Discussions, 2024, 1–23, 2024.

Thilleul, O. and Perignon, Y.: SEM-REV Metocean design basis, Technical report (confidential), 2022.

van der Deijl, W., Schmitt, F., Sicot, C., Barre, S., Hölling, M., and Obligado, M.: Effect of background turbulence on the wakes of horizontal-axis and vertical-axis wind turbines, Journal of Wind Engineering and Industrial Aerodynamics, 253, 105 877, 2024.

https://doi.org/10.5194/wes-2026-160
Preprint. Discussion started: 14 September 2026

VDI: VDI3783-12 Physical modelling of flow and dispersion processes in the atmospheric boundary layer, application of Wind Turbine, Tech. rep., VDI-Platz 1, 40468 Düsseldorf, Germany, 2000.

Wang, C., Campagnolo, F., Canet, H., Barreiro, D. J., and Bottasso, C. L.: How realistic are the wakes of scaled wind turbine models?, Wind Energy Science, 6, 961–981, 2021.